




Column Density Profiles of Cold Clouds Driven by Galactic Outflows

J'Neil Cottle¹, Evan Scannapieco¹ , and Marcus Brüggen²

¹ School of Earth and Space Exploration, Arizona State University, P.O. Box 871404, AZ 85287-1404, USA

² Universität Hamburg, Hamburger Sternwarte, Gojenbergsweg 112, D-21029, Hamburg, Germany

Received 2018 March 31; revised 2018 July 18; accepted 2018 July 21; published 2018 September 4

Abstract

Absorption line studies are essential to understanding the origin, nature, and impact of starburst-driven galactic outflows. Such studies have revealed a multiphase medium with a number of poorly understood features leading to a need to study the ionization mechanism of this gas. To better interpret these observations, we make use of a suite of adaptive mesh refinement hydrodynamic simulations of cold, atomic clouds driven by hot, supersonic outflows, including the effect of radiative cooling, thermal conduction, and an ionizing background characteristic of a starbursting galaxy. Using a new analysis tool, TRIDENT, we estimate the equilibrium column density distributions for 10 different ions: H I, Mg II, C II, C III, C IV, Si III, Si IV, N V, O VI, and Ne VIII. These are fit to model profiles with two parameters describing the maximum column density and coverage, and for each ion we provide a table of these fit parameters, along with average velocities and line widths. Our results are most sensitive to Mach number and conduction efficiency, with higher Mach numbers and more efficient conduction leading to more compact, high column density clouds. We use our results to interpret down-the-barrel observations of outflows and find that the adopted ionization equilibrium model overpredicts column densities of ions such as Si IV and does not adequately capture the observed trends for N V and O VI, implying the presence of strong nonequilibrium ionization effects.

Key words: galaxies: abundances – galaxies: ISM – galaxies: kinematics and dynamics – galaxies: starburst

1. Introduction

It has been quite some time since galaxies have been studied as though they were island universes, growing in isolation by accreting material from their surroundings. Instead, it is now clear that the interactions between galaxies and their surrounding media are much more complex, depending on a network of feedback processes that are powered by stars (e.g., Dekel & Silk 1986; Mac Low & Ferrara 1999; Scannapieco & Broadhurst 2001; Scannapieco et al. 2001; Mori et al. 2002; Scannapieco et al. 2002; Springel & Hernquist 2003; Dalla Vecchia & Schaye 2008; Murray et al. 2011; Hopkins et al. 2012; Creasey et al. 2013; Muratov et al. 2015) and active galactic nuclei (e.g., Scannapieco & Oh 2004; Sijacki et al. 2007; Schaye et al. 2015; Kaviraj et al. 2017). One of the most important of these processes is the exchange of energy and material caused by galactic outflows. These outflows are thought to be driven by star formation and supernovae, (e.g., Heckman et al. 1990; Martin 1999; Shapley et al. 2003; Martin 2005; Veilleux et al. 2005) and can have a significant impact on the evolution of the galaxy, star formation rate, and metallicities (e.g., Tremonti et al. 2004; Oppenheimer et al. 2010; Davé et al. 2011; Agertz & Kravtsov 2015; Lu et al. 2015). Observations provide direct information on the multiphase nature of these outflows (e.g., Sturm et al. 2011; Arav et al. 2013; Bolatto et al. 2013; Meiring et al. 2013; Kacprzak et al. 2014) as well as the composition and dynamics of the circumgalactic medium (CGM) into which they propagate (Keeney et al. 2013; Arribas et al. 2014; Rubin et al. 2014; Werk et al. 2014; Wiseman et al. 2017). However, disentangling the phases of the outflows and understanding their interactions with the environment has proven to be a challenge.

From an analytic perspective, Chevalier & Clegg (1985) derived a solution for a wind being driven from a region of

uniform mass and continuous energy input. This model wind accurately describes the hot regions of galactic outflows observed in X-ray emission (McCarthy et al. 1987). However, these types of observations can only be made for nearby galaxies. For more distant objects, observations are limited to absorption measurements of colder gas, seen either in down-the-barrel observations of the host galaxy's background stellar continuum (Chisholm et al. 2018) or along sightlines through the CGM of starburst galaxies with the background continuum provided by distant quasars (QSOs; Borthakur et al. 2013; Heckman et al. 2017). While the two observations can provide information of the ionization and extent of the CGM, both are significantly limited in their ability to understand the dynamics of the outflowing material. One particular anomaly in observations is the detection of absorption from both high ionization energy ions such as O VI at 138 eV and lower energies like Mg II at 15 eV, with a distinct lack of absorption from N V (e.g., Chisholm et al. 2018). With an ionization energy around 97 eV, N V is expected to be produced in the conditions that produce both O VI and Mg II. This discrepancy has been investigated for nonstarbursting galaxies (Werk et al. 2016), but a cause in relation to starbursting galaxies in particular has yet to be determined. The number of direct observational predictions has been limited, making it unclear to what extent detailed models of the observational properties of cold clouds driven by galactic outflows can explain these trends.

Specifically, numerical simulations have focused on the nature of the outflowing material and the physics dominating the interaction between winds and cooler clouds. Klein et al. (1994) have shown results for hydrodynamical simulations in which clouds within these winds were found to be accelerated and elongated over timescales longer than the time required for the shock to cross the cloud—demonstrating the need for longer simulations to fully understand the cloud evolution.

Since then, numerical simulations have expanded to investigate cloud–wind interactions from many angles from studies, including thermal conduction and radiative cooling (e.g., Orlando et al. 2005; Schneider & Robertson 2017; Gronke & Oh 2018), accounting for nonequilibrium chemistry effects (e.g., Kwak et al. 2011) and incorporating magnetic fields (e.g., Mac Low et al. 1994; Fragile et al. 2005; McCourt et al. 2015). Even so, these simulations have not covered the full parameter space relevant to galactic outflows and have not yet been directly connected to likely observations.

There have been several attempts to derive absorption line properties from cosmological simulations that include outflows (e.g., Oppenheimer & Davé 2006; Oppenheimer et al. 2009; Ford et al. 2013; Turner et al. 2016). However, these studies did not look at cold cloud properties with isolated outflows. Simulations of isolated cloud–wind systems have focused on the hydrodynamic interactions with less attention to the possible connections to observations. In addition, attempts to explain possible models for the spectra and absorption profiles observed fall short of having reliable ways to connect to simulations already performed.

New analytic tools, such as TRIDENT (Hummels et al. 2017), can help bridge the gap between simulations and observations. This can be done by generating synthetic spectra and calculating ion number densities within simulations without the extra computational cost of including a chemistry solver. For this work, we explore the possibility of generating column densities of commonly observed ions from existing simulations with TRIDENT in order to make comparisons between simulation results and actual outflow observations.

In this paper, we present synthetic column density calculations and velocity profiles of clouds simulated with both radiative cooling and thermal conduction at various evolutionary stages. In Section 2, we discuss the simulations used within this study including the parameters and relevant physics. In Section 3, we outline the methods of calculating the column density and velocity profiles as well as the procedure for fitting profiles for each cloud. Section 4 includes comparisons across simulation parameters and ion species, with an application of these results to observations in Section 5. We conclude with a discussion and motivation for future work in Section 6.

2. Simulations

We performed a full analysis of the ion densities on the outflow simulations in Scannapieco & Brüggén (2015) and Brüggén & Scannapieco (2016), SB15 and BS16, respectively, hereafter. This suite of simulations was carried out with FLASH (version 4.2) (Fryxell et al. 2000), a multidimensional hydrodynamics code that solves the fluid equations on a Cartesian grid with a directionally split Piecewise-Parabolic Method (Colella & Woodward 1984). The simulations were done in three dimensions, as limiting the degrees of freedom can influence the development of shear instabilities. They assumed an initial cloud radius of 100 parsec, a temperature of 10^4 K, a mass density of $\rho = 10^{-24}$ g cm $^{-3}$, and a mean atomic mass of $\mu = 0.6$. These parameters result in a total column density of 3.1×10^{21} cm $^{-2}$. As shown below, this column density determines cloud evolution, rather than the radius and density.

Initially, the cloud was positioned at (0, 0, 0) within the domain covering a physical volume of -800×800 parsecs in the x and y directions and -400×800 parsecs in the z

direction, which was the direction of the hot outflowing material. The interaction at the z boundary was defined by a condition where the incoming material is added to the grid and given the same values of density, v_{hot} , and $c_{s,\text{hot}}$ as the initial conditions. For all other boundaries, the FLASH “diode” condition was used, which assumes the gradient normal to the edge of the domain of all variables except pressure to be zero and only allows material to flow out of the grid.

2.1. Physics of Cloud Evolution

Two important timescales that influence the evolution of a cold cloud embedded within a hot wind and the cloud crushing time, t_{cc} , and the cooling time, t_{cool} . The cloud crushing time effectively describes the amount of time it would take the initial shock to travel halfway through the cloud and is given by

$$t_{\text{cc}} = \frac{R_c}{v_{\text{hot}} \chi_0^{1/2}}, \quad (1)$$

which is dependent only on the velocity of the wind, v_{hot} , and the density ratio, χ_0 (e.g., Klein et al. 1994). The cooling time, which determines the time for the cloud to radiate away its thermal energy, is given by

$$t_{\text{cool}} = \frac{(3/2)n_c kT}{\Lambda(T)n_e n_{i,c}}, \quad (2)$$

where T is the temperature, $\Lambda(T)$ is the equilibrium cooling function at T with n_c , and $n_{e,c}$ and $n_{i,c}$ are the total, electron, and ion number densities within the cloud. If the ratio of $t_{\text{cool}}/t_{\text{cc}} = N_{\text{cool}}/(n_{i,c}r_c)$ with $N_{\text{cool}} \equiv 3kTn_v(2\Lambda\chi^{1/2}n_{e,c})^{-1}$ is below one, then cooling will have a significant influence on the evolution of the cloud. Table 1 in SB15 gives values for N_{cool} as calculated using equilibrium cooling curves from Wiersma et al. (2009) assuming solar metallicity and a mean molecular mass of 0.6. With column densities between 10^{17} and 10^{19} cm $^{-2}$, the resulting ratio between cooling time to cloud crushing time is small. For the range of parameters used, the clouds are able to cool on a timescale much shorter than the timescale for the evolution of the cloud allowing for cooling to influence the cloud before it is disrupted by the shock.

Within the simulations, cooling was computed in the optically thin limit assuming local thermodynamic equilibrium

$$\dot{E}_{\text{cool}} = (1 - Y) \left(1 - \frac{Y}{2}\right) \frac{\rho \Lambda}{(\mu m_p)^2}, \quad (3)$$

where \dot{E}_{cool} is the radiated energy per unit mass, ρ is the density in the cell, m_p is the proton mass, $Y = 0.24$ is the helium mass fraction, $\mu = 0.6$ is the mean atomic mass, and $\Lambda(T, Z)$ is the cooling rate as a function of temperature and metallicity. With the assumption that the abundance ratios of the metals are always solar, the tables compiled by Wiersma et al. (2009) were used. Heating by a photoionizing background was not included in the calculations; however, subcycling was implemented (Gray & Scannapieco 2010) along with a cooling floor at $T = 10^4$ K.

The fluid equations, including thermal conduction and radiative cooling, as solved by FLASH are

$$\partial_t \rho + \nabla \cdot (\rho \mathbf{u}) = 0, \quad (4)$$

$$\rho [\partial_t \mathbf{u} + (\mathbf{u} \cdot \nabla) \mathbf{u}] = -\nabla p, \quad (5)$$

$$\partial_t E + \nabla \cdot [Eu] = -\nabla \cdot (p\mathbf{u}) - n^2 \Lambda(T) + \nabla \cdot \mathbf{q}, \quad (6)$$

where ρ is the density, \mathbf{u} is the velocity, $p = k_B T \rho / (\mu m_p)$ is the pressure, $E = p/(\gamma - 1) + \frac{1}{2} \rho |\mathbf{u}|^2$ is the total energy density, $\Lambda(T)$ is the radiative cooling function, and \mathbf{q} describes the heat flux due to conduction. We adopt a saturated thermal conduction limit when the mean-free path of electrons is much larger than the length scale of the temperature gradient. This leads to the definition

$$\mathbf{q} = \min(\kappa(T) \nabla T, \quad 0.34 n_e k_B T c_{s,e} \nabla T |\nabla T|), \quad (7)$$

(Cowie & McKee 1977), where $\kappa(T) = 5.6 \times 10^{-6} T^{5/2} \text{ erg s}^{-1} \text{ K}^{-1} \text{ cm}^{-1}$ and $c_{s,e} = (k_B T / m_e)^{1/2}$ is the isothermal sound speed of the electrons in the wind with m_e being the mass of the electron. It is assumed that electrons and ions have the same temperature. The diffusion equation describing conduction is then solved with the general implicit diffusion solver in FLASH. Saturated thermal conduction was also implemented with the use of a flux limiter that modifies the diffusion coefficient to vary until some maximum flux, as determined by the Larsen flux limiter (Morel 2000). In units of cloud crushing times, these equations are invariant under the transformation

$$\mathbf{x} \rightarrow \alpha \mathbf{x}, \quad t \rightarrow \alpha t, \quad \text{and} \quad \rho \rightarrow \alpha \rho, \quad (8)$$

resulting in the evolution of the cloud only depending on the product of the size and density.

2.2. Selection of Evolutionary Stages

While the cloud crushing time is a good description of the disruption time for a single cloud, this study compares evolutionary stages across many types of clouds. To compare to t_{cc} , another timescale is defined over the course of the cloud's evolution based on the mass fraction of the cloud that is at or above one-third of the cloud's original density. The first time, t_{95} , corresponds to the time at which 95% of the cloud is at or above this density. The following three times, t_{75} , t_{50} , and t_{25} follow a similar pattern with 75%, 50%, and 25% of the cloud. These four stages correspond to the four evolutionary stages we consider while estimating column densities.

2.3. Frame Changing and Refinement/Derefinement

In order to follow the disruption of the clouds, it was necessary for the simulations to shift frames as the cloud drifts through the wind. To do this, SB15 and BS16 have implemented an automated frame change routine (see SB15 and BS16 for details). In addition, they used FLASH's default variables of temperature and density with a refinement criterion on 0.8. A secondary refinement condition was enforced to ensure the simulation maintained high resolution in areas important to cloud evolution and to reduce the computational cost of higher refinement in areas of the simulation that have less influence on the cloud evolution. This additional condition imposed derefinement on cells that satisfied one of the following: (1) the cell was outside of a cylinder along the z axis with radius three times the initial cloud radius or nine times the current x extent of the cloud or (2) the cell was outside of a cylinder centered on the z axis with radius equal to the initial cloud radius or three times the current x extent of the cloud and

both the distance to the x - y plane and the z center of the cloud were greater than three times the current radius of the cloud.

2.4. Parameters

The parameter space for these simulations is reduced to the wind parameters; T_{hot} , v_{hot} , and column density of the cloud. According to Chevalier & Clegg (1985), Mach number depends only on r/R_* , where r is the distance from the outflowing region and R_* is the driving radius of the flow. This radius reflects the size of the region in which the energy input from sources such as supernovae accelerates the gas. At the edge of this region, the gas becomes supersonic and tends to a constant velocity at further radii. For M82, $R_* \approx 300 \text{ pc}$ (McKeith et al. 1995). It follows that the energy and mass input from the wind can be fully described with the velocity of the hot medium, while the Mach number corresponds to sampling the wind as a function of radius. For the Mach numbers considered, assuming $R_* = 300 \text{ pc}$, the physical scale of these radii ranges from 0.3 to 2.9 kpc from the central starburst. For the cloud with a temperature corresponding to the minimum temperature attainable with atomic cooling ($\approx 10^4 \text{ K}$), the Jeans length for this gas is $\lambda_J \approx 2 \text{ kpc}$, much larger than the size of the clouds considered, indicating that the clouds must be confined by pressure to keep from expanding. The pressure equilibrium then requires the ratio of the cloud density to the wind density, χ_0 , to be equal to the ratio of the temperature of the wind to the temperature of the cloud.

The choices for T_{hot} and v_{hot} , as well as the corresponding density contrast and cloud crushing times, for a cloud radius of 100 parsec are given in Table 1 for both the cooling and conduction runs. The Mach number of the hot wind, M_{hot} , is also given. The naming scheme of the runs describes Mach number, wind velocity, and wind temperature in order, with suffixes denoting other unique traits of the run. The parameters were chosen to focus on regions outside of the driving radius, $r > R_*$, with Mach numbers ≥ 1 and provide multiple runs with the same temperatures and velocities to study the impact of changing the Mach number within the hot wind. Also included are runs with both wind and cloud densities 10 times greater than their original counterparts (named with the -hc suffix) and one low conduction run with one-third the *Spitzer* value used in all other conduction runs (named with a -lc suffix).

3. Estimation of Observables

3.1. Trident Analysis

Our analysis makes use of the TRIDENT analysis tool (Hummels et al. 2017), an extension of the yt analysis code (Turk et al. 2011). TRIDENT is a multifunctional tool created to enable simulated observations of astronomical hydrodynamic simulations. It can be used to create absorption line spectra through simulated data sets as well as column density maps for ion species not originally within the simulation outputs. The full description of the code can be found in Hummels et al. (2017). However, a short description of the relevant details is given here.

In order to generate density maps and spectra, TRIDENT first calculates the density of a given ion within the simulated data set. This is done through the module `ion balance`. The module first determines if the data set contains a density element for each cell within the domain considered, this may be the entire data set or a subset representing a sightline as defined by TRIDENT's `LightRay`. If the simulation explicitly tracks

Table 1
Simulation Parameters—Conduction Runs End in -c; High Column in -hc; Low Conduction in -lc

Name	Conduction	M_{hot}	v_{hot} (km s ⁻¹)	T_{hot} (10 ⁶ K)	T_{hot} (keV)	χ_0	t_{cc} (Myr/100 pc)
M0.5-v430-T3		0.5	430	30	2.7	3000	12.5
M1-v480-T1		1	480	10	0.86	1000	6.4
M1-v860-T3		1	860	30	3.7	3000	6.2
M1-v1500-T10		1	1500	100	8.6	10000	6.5
M3.8-v1000-T0.3		3.8	1000	3	0.27	300	1.7
M3.5-v1700-T1		3.5	1700	10	0.86	1000	1.8
M3.6-v3000-T3		3.6	3000	30	2.7	3000	1.8
M6.5-v1700-T0.3		6.5	1700	3	0.27	300	1.0
M6.2-v3000-T1		6.2	3000	10	0.86	1000	1.0
M11.4-v3000-T0.3		11.4	3000	3	0.27	300	0.56
M1-v480-T1-c	✓	1	480	10	0.86	1000	6.4
M1-v860-T3-c	✓	1	860	30	3.7	3000	6.2
M1-v1500-T10-c	✓	1	1500	100	8.6	10000	6.5
M3.8-v1000-T0.3-c	✓	3.8	1000	3	0.27	300	1.7
M3.5-v1700-T1-c	✓	3.5	1700	10	0.86	1000	1.8
M3.6-v3000-T3-c	✓	3.6	3000	30	2.7	3000	1.8
M6.5-v1700-T0.3-c	✓	6.5	1700	3	0.27	300	1.0
M11.4-v3000-T0.3-c	✓	11.4	3000	3	0.27	300	0.56
M3.8-v1000-T0.3-hc	✓	3.8	1000	3	0.27	300	1.7
M3.5-v1700-T1-hc	✓	3.5	1700	10	0.86	1000	1.8
M3.6-v3000-T3-hc	✓	3.6	3000	30	2.7	3000	1.8
M6.5-v1700-T0.3-lc	✓	6.5	1700	3	0.27	300	1.0

the ion’s density through a chemistry solver, this density is used. However, for this paper, each ion number density is derived from the gas density and metallicity fields within the data set and an ionization fraction assuming ionization equilibrium. The final estimation for the number density of the i th ion of element X becomes

$$n_{X,i} = f_{\text{H}} \frac{\rho}{m_{\text{H}}} Z \left(\frac{n_X}{n_{\text{H}}} \right)_{\odot} f_{X,i}, \quad (9)$$

where ρ and Z are the gas density and metallicity fields, respectively, from the data set, f_{H} is the primordial H mass fraction with an adopted value of 0.76, and $Z \left(\frac{n_X}{n_{\text{H}}} \right)_{\odot}$ is the solar abundance.

3.2. UV Background

The equilibrium ionization fraction, $f_{X,i}$, is a function of temperature, density, and incident radiation, most typically a UV metagalactic background. For use within the `ion balance` module the ionization fraction is linearly interpolated over a grid of precalculated ionization fractions through temperature, density, and redshift. The default UV background for TRIDENT is the Haart & Madau (2012) metagalactic background. While this is appropriate for approximating the ions within the intergalactic medium, it is not an accurate estimation of the environment around starburst galaxies.

In order to create a new ionization fraction lookup table to integrate with TRIDENT, the shape and intensity of the incident radiation was based off of a STARBURST99 model (Leitherer et al. 1999). Here we used the best-fit theoretical model found within Chisholm et al. (2018) from “down-the-barrel” observations of the outflow in galaxy J1226+2152. Such an orientation allowed for the absorption lines of the ISM to be embedded within the stellar continuum. The best-fit

model was found by fitting both the continuum and extinction using a Calzetti extinction law (Calzetti et al. 2000). The STARBURST99 models make use of the Geneva stellar evolution model and varied interstellar continuum metallicities. The best-fit model had a stellar metallicity of 0.2 Z_{\odot} and a light-weighted age of 11 Myr. With the shape of the incident radiation given by the best-fit STARBURST99 model, the strength of the radiation is dependent on the distance from the source, which we infer from the measured ionization parameter in Chisholm et al. (2018), $\log(U) = -2$.

The construction of the table then followed the same procedure as outlined in Smith et al. (2008, 2017). Ionization fractions were computed within a grid containing temperature, hydrogen number density, and redshift. While redshift was not explicitly taken into account, these results are applicable to observations with $z \geq 0$ due to the fact that this analysis focused on the influence of the dominant starburst background, which is redshift independent. The grid was populated with calculations using the photoionization software, CLOUDY (Ferland et al. 2013), which takes the best-fit STARBURST99 model as the shape of incident radiation and an ionization parameter of $\log(U) = -2$ (see Chisholm et al. 2018). These simulations spanned a range of temperatures from 10 to 10⁹ K in step sizes of 0.025 dex, and hydrogen number densities 10⁻⁹–10⁴ cm⁻³ in step sizes of 0.125 dex, to mimic the default table within TRIDENT, and to allow for integration with the existing TRIDENT procedure with little modification. The newly generated table was then loaded in place of the default ionization table and ion number densities were calculated as described above.

With the use of the new table, column density maps can be created as shown in Figure 1. These projections are for the M3.8-v1000-T0.3-c and M3.8-v1000-T0.3 runs highlighting the difference in structure between the conduction and cooling runs. While conduction creates dense clouds, runs without conduction are much more diffuse with more coverage. With

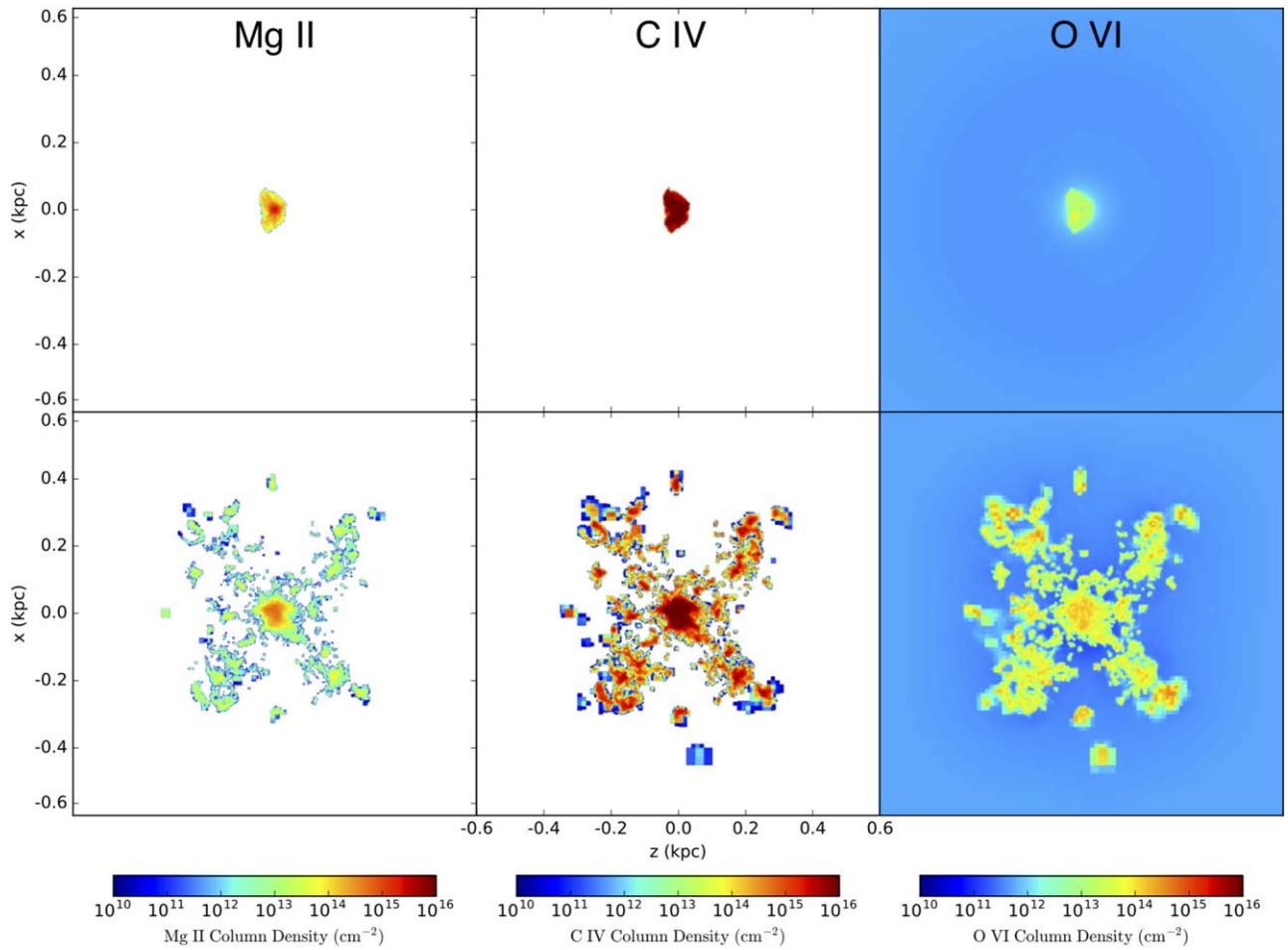


Figure 1. Density projections down-the-barrel (through the wind), for Mg II (left), C IV (middle), and O VI (right) at t_{50} for the M3.8-v1000-T0.3 runs. The efficient conduction run is shown in the top panels and inefficient conduction is shown in the bottom panels.

the inclusion of conduction, higher column densities are more possible than those that can result from shock-induced ionization. For these runs, compression by the evaporative flow is most significant at low Mach numbers and low density contrasts. However, as BS16 note, evaporative compression influences all runs producing small dense clouds at late times in parallel with the streamwise pressure gradient stretching the clouds into filaments. While the filaments are created in the runs with radiative cooling and inefficient conduction, it is this evaporation that leads to such different morphologies between the two sets of simulations. If conduction is suppressed by factors such as magnetic fields, the radiative cooling runs may lead to clouds more descriptive of the accelerated material in outflows.

The multiphase nature of these outflows can be seen by looking at the average temperature for each ion. In Figure 2, the distribution of average temperature across all runs and times for ions of various ionization potentials is shown. Despite the wide range of wind parameters, there is a distinct distribution of temperatures for each ion. It is particularly interesting that the average temperature for O VI and N V are substantially higher than the temperature of the cloud, indicating that these ions are produced in a separate phase than the low and intermediate ionization potential ions such as Mg II and Si IV. These high temperatures imply that the higher ionization potential ions are primarily collisionally ionized within these simulations.

3.3. Column Density Profiles

The column density for each projection along the sightline for each ion at any stage was computed as

$$N = \int_{\text{los}} n_i(z) dz, \quad (10)$$

where $n_i(z)$ is the number density of ion, i , and z is the direction of the projection.

We considered a down-the-barrel projection representative of outflows for all runs. Each projection was taken at a fixed resolution of 800×800 cells for the domain covering $1.6 \text{ kpc} \times 1.6 \text{ kpc}$, resulting in one pixel per 4 pc^2 . At this resolution, the initial cloud area within the simulation covered 0.0314 kpc^2 , or 7880 cells. For each cell, we ranked the column densities from lowest to highest and took the top 7880 to give a profile of the column densities that cover a simulation area equal to the initial cloud area. An example of this profile can be seen in Figure 3. We determine that the profiles can be described by the functional form

$$N(x) = N_0 \frac{0.01}{1.01 - x^q}, \quad (11)$$

where x is the fractional rank of each cell expressed as a fraction of the total pixels and N_0 translates to an upper limit on column density for the cloud and q expresses the degree to which the cloud has been compacted. A high q relates to a very

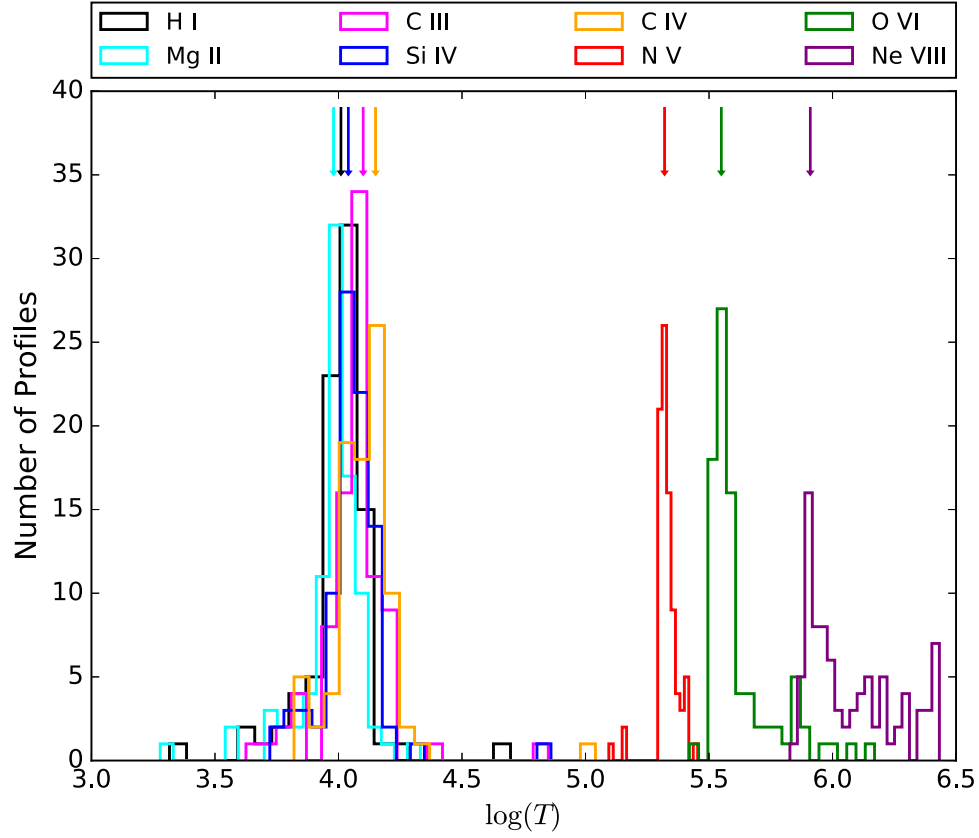


Figure 2. Distribution of average temperatures for eight ions; H I, Mg II, C III, C IV, Si IV, N V, O VI, and Ne VIII over all times and runs. An approximate average temperature for each ion is highlighted with an arrow above the distribution.

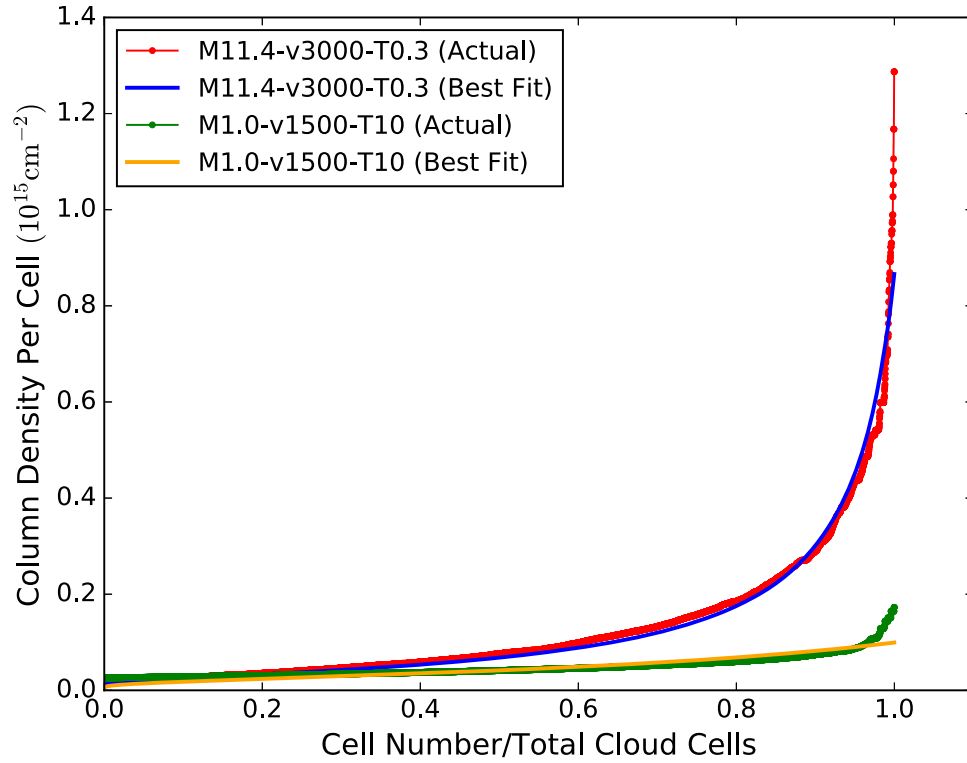


Figure 3. Sample of the column density profile with the best-fit line overplotted. Two runs are shown at t_{75} for the ranked column density of O VI; M11.4-v3000-T0.3 (actual in red, best-fit in blue) and M1.0-v1500-T10 (actual in green, best-fit in yellow). The best-fit overplotted is the functional form of Equation (11) with the best-fit parameters $N_0 = 8.68 \times 10^{14} \text{ cm}^{-2}$ and $q = 0.18$ for the M11.4-v3000-T0.3 run and $N_0 = 9.94 \times 10^{13} \text{ cm}^{-2}$ and $q = 0.02$ for the M1.0-v1500-T10 run.

Table 2
Sample of Table of Best-fit Parameters q and τ —C IV

Run	Velocity (km s ⁻¹)	b (km s ⁻¹)	N_0 (cm ⁻²)	Upper N_0 Err	Lower N_0 Err	q Fit	Upper q Err	Lower q Err	Average N (cm ⁻²)	Average N Err
M3.8-v1000-T0.3-c	22	971	2.813e+17	3.179e+9	2.813e+17	1.925	24.641	4.180e-08	8.586e+15	7.410e+6
M3.8-v1000-T0.3-c	36	912	1.140e+17	1.424e+9	1.140e+17	0.725	20.688	1.559e-08	6.507e+15	2.321e+7
M3.8-v1000-T0.3-c	61	869	1.091e+17	9.405e+8	1.091e+17	1.099	19.531	1.628e-08	4.734e+15	2.467e+7
M3.8-v1000-T0.3-c	110	777	3.724e+16	3.396e+8	3.724e+16	0.517	28.297	8.347e-09	2.666e+15	2.821e+6
M3.6-v3000-T3-c	21	62	1.535e+16	1.260e+13	1.535e+16	0.019	47.396	6.820e-07	7.185e+15	3.632e+6
M3.6-v3000-T3-c	14	36	7.317e+17	8.702e+10	7.317e+17	6.007	20.083	1.640e-3	1.252e+16	3.824e+7
M3.6-v3000-T3-c	43	80	1.610e+17	2.122e+9	1.610e+17	1.155	26.605	2.650e-08	6.765e+15	4.003e+7
M3.6-v3000-T3-c	39	73	1.185e+18	2.859e+10	1.185e+18	14.060	14.276	1.136e-1	1.549e+16	1.840e+8
M3.5-v1700-T1-c	13	118	2.196e+16	4.838e+11	2.196e+16	0.037	49.787	1.229e-05	7.629e+15	2.745e+6
M3.5-v1700-T1-c	21	116	1.182e+17	1.154e+9	1.182e+17	0.613	23.710	7.903e-09	7.548e+15	7.335e+7
M3.5-v1700-T1-c	27	143	5.673e+17	5.985e+9	5.673e+17	6.032	13.455	2.156e-06	9.695e+15	3.111e+7
M3.5-v1700-T1-c	36	107	3.829e+17	5.077e+9	3.829e+17	6.894	11.566	2.551e-3	6.215e+15	6.473e+3
M3.8-v1000-T0.3	108	787	4.291e+16	5.257e+9	4.291e+16	0.220	36.217	1.331e-08	5.399e+15	2.070e+7
M3.8-v1000-T0.3	143	679	4.051e+16	6.549e+9	4.051e+16	0.245	26.992	2.333e-09	4.755e+15	1.464e+7
M3.8-v1000-T0.3	158	637	3.315e+16	3.066e+8	3.315e+16	0.205	32.308	2.917e-08	4.352e+15	1.893e+7
M3.8-v1000-T0.3	204	613	9.625e+15	3.212e+13	9.625e+15	0.065	47.141	8.882e-06	2.514e+15	2.935e+7
⋮	⋮	⋮	⋮	⋮	⋮	⋮	⋮	⋮	⋮	⋮

compact cloud along the line of sight, while a low q is more descriptive of a diffuse cloud along the line of sight or a consistent column density throughout the entire simulation area considered. This parameter can also be thought of as an analog for coverage, with high q translating to a small amount of coverage with nearly maximum column density cells and low q describing greater coverage of the sightline containing high column density cells.

We found the posterior probability distributions of the parameters N_0 and q with an Affine Invariant Markov Chain Monte Carlo Ensemble sampler through the use of the Python package `emcee` developed by Foreman-Mackey et al. (2013). With the use of priors, N_0 and q were restricted to values between 0 and twice the maximum column density in the domain and 0 and 100, respectively. The 1σ errors were then derived from the 16th and 84th percentile contours of the posterior.

It is also informative to consider a total average column density. However, as the column density profiles have been cast into a space relating to a fraction of the initial cloud area (x), this average is restricted to considering this specified simulation area rather than the entire cloud. An average column density over a simulation area equal to the size of the initial cloud area was therefore calculated as a proxy for total average column density. This was determined numerically from the best-fit model profile as

$$N_{\text{total}} = \int_0^1 N_0 \frac{0.01}{1.01 - x^q} dx. \quad (12)$$

The column density of a portion of the cloud can be found in a similar way, changing the limits of integration to reflect the portion of the cloud considered. The average column density over the densest half of the cloud corresponds to the value of the integral above with limits from 0.5 to 1. The average column density, along with the best-fit parameters and the corresponding errors, was stored in a lookup table.

Also calculated was the average velocity of each ion as well as an estimate of the width of an approximate Gaussian profile, or b parameter, including both the thermal velocity spread (b_t)

and contribution of Doppler broadening (b_d). The average velocity, weighted by the ion number density, was calculated as

$$\bar{v}_i = \frac{\int n_i(x, y, z) v(x) dV}{\int n_i(x, y, z) dV}. \quad (13)$$

Again, with x being the direction along the line of sight. The b parameter was estimated to be the average of the b calculated for all sightlines for the given projection, expressed as $b = \langle \sqrt{b_t^2 + b_d^2} \rangle$, with

$$b_t^2 = \frac{\int \frac{2k_b T(x, y, z)}{\mu_i m_p} n_i(x, y, z) dx}{\int n_i(x, y, z) dx} \quad (14)$$

and

$$b_d^2 = \frac{\int (v(x) - \bar{v}_i)^2 n_i(x, y, z) dx}{\int n_i(x, y, z) dx}. \quad (15)$$

Here $T(x, y, z)$ is the temperature of the gas and μ_i , the mass number of the ion and m_p , the mass of a proton, with all other constants defined in the usual form. The values for \bar{v}_i and b are stored within the table of best-fit parameters.

This table was created for 10 different ions, including low ionization energies prevalent within the cool cloud material, such as H I and Mg II through intermediate energies, Si III, Si IV, C II, C III, C IV, and N V to those at the high end, O VI and Ne VIII. These best-fit parameters and the associated errors are quoted in 10 digital tables, one for each ion considered. Table 2 represents a sample of these tables. The full tables are available online.³

4. Results

The distribution of the best-fit parameters, N_0 and q , for the down-the-barrel projections are shown in Figures 4 and 5. Of the 10 ions, 8 are shown, excluding C II and Si III, which are useful for connections to observations but show little to no

³ <http://www.public.asu.edu/~jcottle1/coldensprofiles.html>

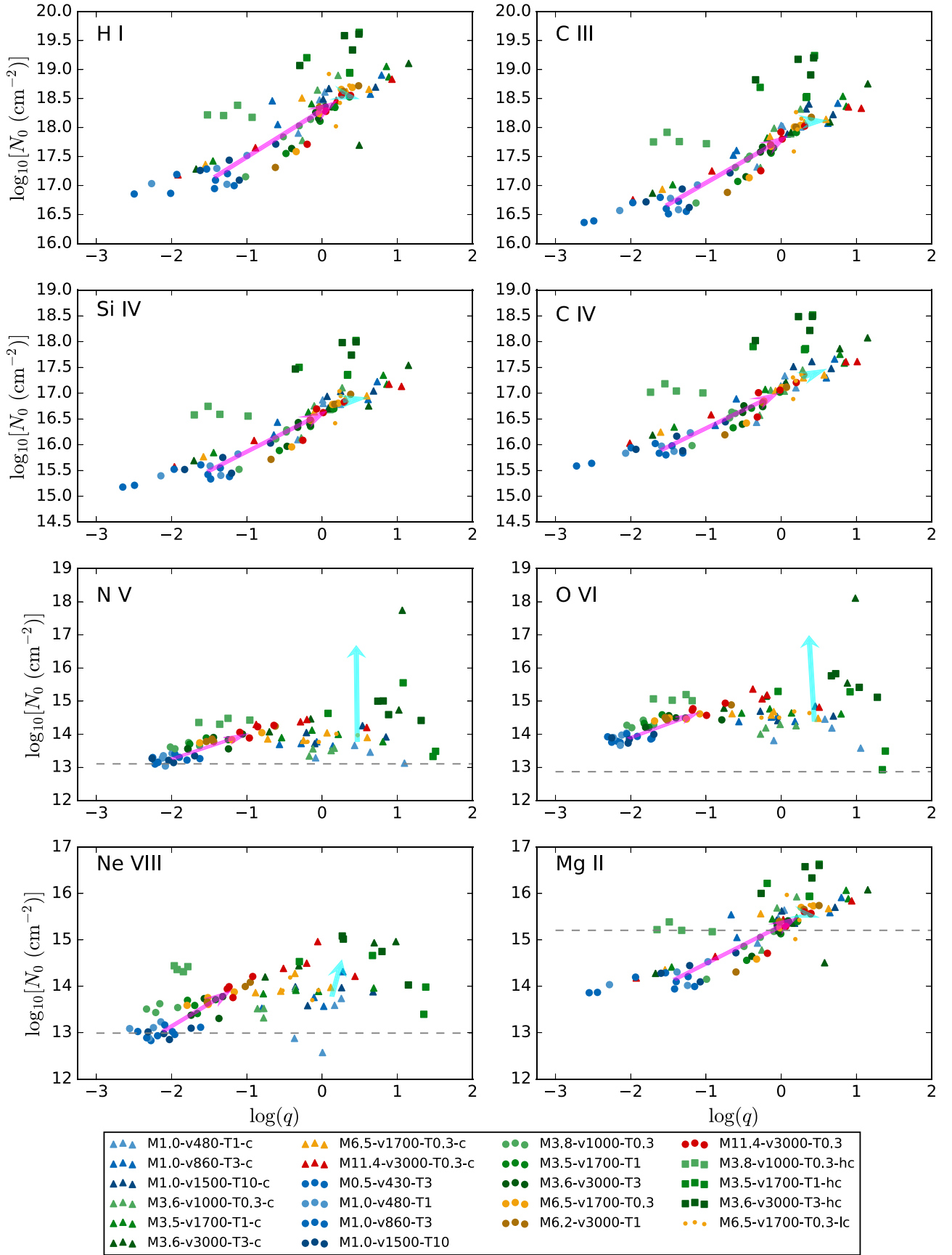


Figure 4. Distribution of N_0 and q parameters in log space for all runs and eight ions. Runs are color coded by Mach number with the lowest Mach numbers being in shades of blue and the highest Mach numbers in shades of red. Cooling and conduction runs are marked by circles and triangles, respectively. Also shown are the high column density runs (squares) and the low conduction run (small dots). Arrows (magenta for cooling and cyan for conduction) are overlaid to highlight the trends discussed in Sections 4.1 and 4.2. Dashed lines indicate observational limits on column densities.

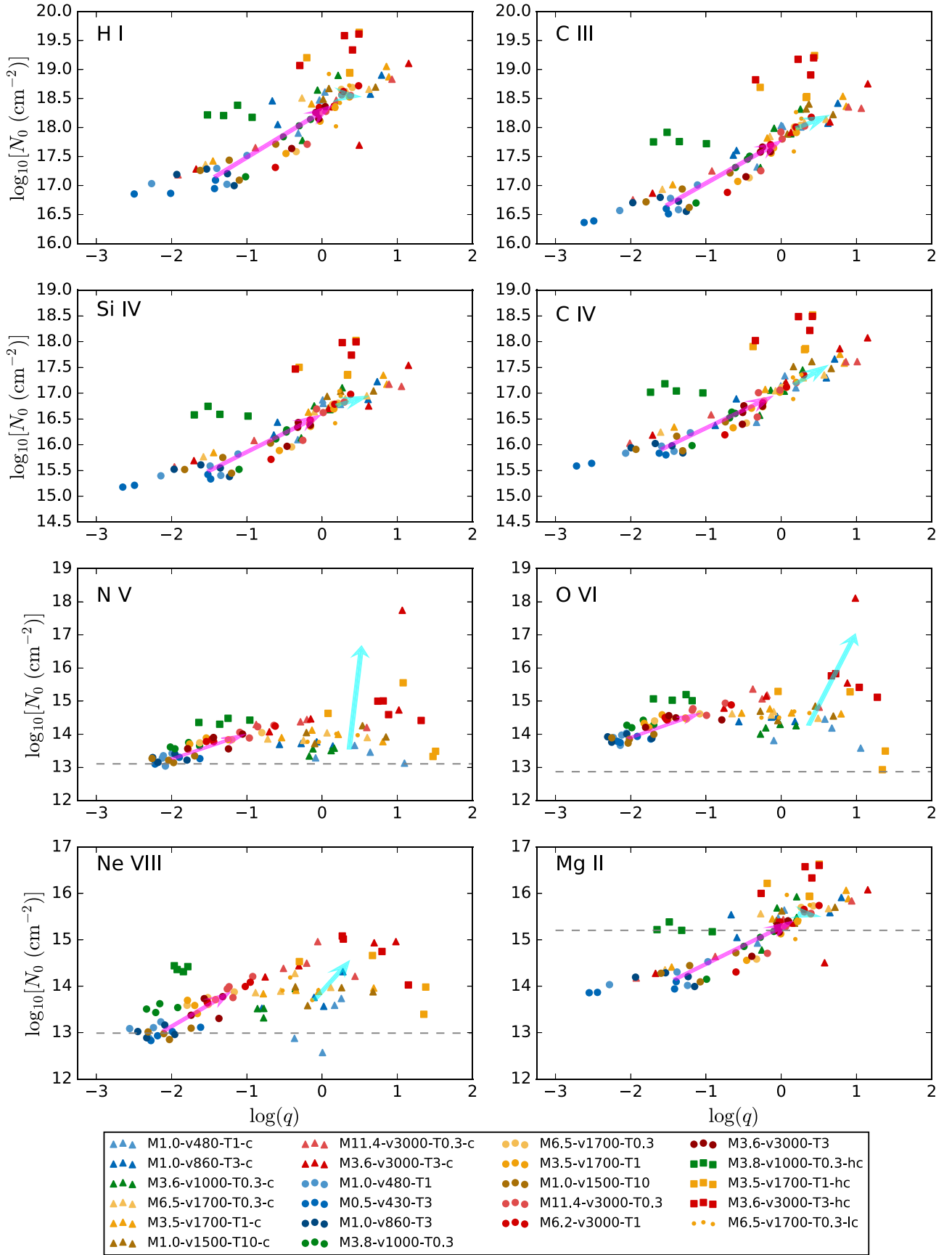


Figure 5. Distribution of N_0 and q parameters in log space for all runs and eight ions. Runs are color coded by wind velocity with the lowest velocities in shades of blue and the highest velocities in shades of red. Similar to Figure 4, cooling and conduction runs are marked by circles and triangles, respectively. Also shown are the high column density runs (squares) and the low conduction run (small dots). Arrows (magenta for cooling and cyan for conduction) are overlaid to highlight the trends discussed in Sections 4.1 and 4.2. Dashed lines indicate observational limits on column densities.

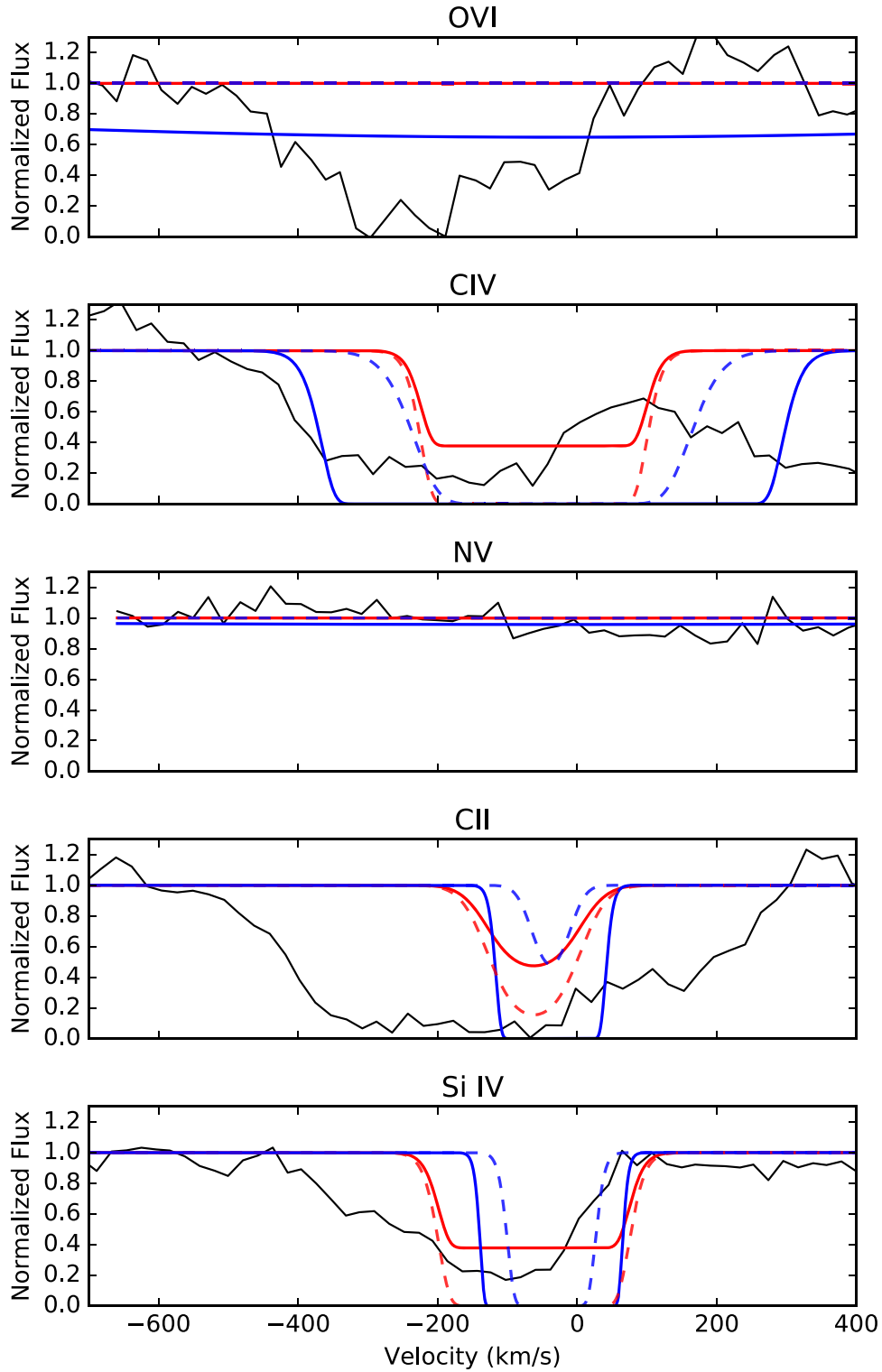


Figure 6. Best-fit absorption profiles to the Chisholm et al. (2018) observations (shown in black) for the multicloud (blue) and covering fraction (red) cases shown for one characteristic time, t_{25} . The covering fraction best fits correspond to the run M3.5-v1700-T1. The multicloud best fits correspond to the run M3.6-v3000-T3-hc. Also shown in dashed lines are the profiles with $\alpha = 1$ (blue dashed) and $f = 1$ (red dashed) for the same runs.

variation from the distributions seen with C III. Within both figures, the best-fit parameters for all four times of each run are plotted. The colors are indicative of either the Mach number (Figure 4) or wind velocity (Figure 5). While these two parameters are related, they affect the results somewhat differently and are the most informative of the simulation

parameters. There is no trend with wind temperature. Inefficient conduction runs are denoted with circular markers while runs with conduction are denoted with triangular markers. Trends with increasing Mach number (Figure 4) and wind velocity (Figure 5) for these subsets are shown with magenta (cooling) and cyan (conduction) arrows. A limiting observable column

Table 3Estimated Limiting Column Densities for a 3σ Detection with an SNR of 10

Ion	$\log_{10} N$
H I	12.38
Mg II	15.206
C II	12.88
Si III	14.66
Si IV	12.59
C III	12.11
C IV	12.72
N V	13.107
O VI	12.87
Ne VIII	12.99

density can be estimated with the equivalent width, $W = N\lambda f$, where we assume an SNR of 10 and a velocity width of 100 km s^{-1} . For a detection at 3σ , these column densities range between $\log_{10}(N) \approx 12$ for ions such as H I and C IV to $\log_{10}(N) \approx 15$ for Mg II and Si III. They are listed in Table 3. The best-fit column densities are well above these limits for most ions. However, for the ions where the fits are in the neighborhood of the observation limits, Mg II, N V, O VI, and Ne VIII, dashed lines have been included in Figures 4 and 5 for reference.

4.1. Conduction versus Cooling

Most notably, the majority of the conduction runs span a distinctly different portion of parameter space than the low Mach number runs without conduction. In particular, for low ionization ions such as Mg II, C III, C IV, and Si IV the runs with inefficient conduction span a lower range of q values than the conduction runs, as demonstrated by the much shorter lengths of cyan arrows for these ions as opposed to the magenta arrows. As low q corresponds to little compaction or high coverage, it is seen clearly here that the cloud material, where much of these ions originate is sparse and diffuse for the runs with inefficient conduction. Additionally, for the lower ions, the values for N_0 for the inefficient conduction runs tend to be lower than the runs with efficient conduction at low and mid Mach numbers.

For higher ionization ions, O VI and N V, the distinction between cooling and conduction runs is seen in the q parameter. High values of q , corresponding to very compact clouds or little coverage, are dominated by the conduction runs while the runs with inefficient conduction stay within the diffuse cloud regime. If these ions are primarily produced on the boundary of the cloud, as is implied by the fact that these ions trace higher temperatures than the core of the cloud (Figure 2), the q parameter for these ions reflects the thickness of these boundaries where these intermediate ions are produced. The cooling and conduction runs have ranges for maximum column density that are consistent with each other. Cooling runs with high velocities appear to have comparable maximum column densities to the conduction runs. It appears that conduction does not significantly influence the amount produced of these ions but may in general produce smaller amounts of coverage.

For the highest ionization energy, Ne VIII, there is even more defined clustering between the cooling and conduction runs, primarily dictated by the q parameter. Cooling runs tend toward low q fits while conduction runs exist on the higher end of the q

parameter but span a similar range of N_0 . For runs with inefficient conduction, the Ne VIII column density is more dependent on the Mach number while for the conduction runs, the larger column densities correlate with higher velocities.

4.2. Mach Number and Velocity

As seen most clearly in Figure 4, the Mach number of the wind has a strong influence on the column density profile. Consistently for all ions, the lowest Mach numbers result in the least compact and lowest density profiles and the highest Mach numbers result in the most compact clouds. While it is the tendency for high Mach numbers to compress the cloud, which would result in a higher maximum column density, this trend is mostly seen in the runs with inefficient conduction. For the conduction runs, the higher Mach numbers do not influence N_0 . This is especially apparent when considering that the conduction trend arrows for the Mach number do not follow the data as closely as the cooling trend arrows. This is due to conduction runs producing a dense, thin, filament along the flow of the wind, which becomes thinner and more extended as the Mach number increases. This is not seen for the runs with inefficient conduction because high Mach numbers produce similar cloudlets to low Mach numbers, but with higher densities.

This compression of the cloud due to higher Mach number winds strongly influences the runs with inefficient conduction. It is most evident in the panels for N V and O VI. Here there is little change in the amount of each ion produced, as the N_0 has little variation. However, the best fits for q follow a trend from low to high with increasing Mach number—within the cooling simulations. The compression of the conduction runs is much less dependent on Mach number as the lowest Mach number runs (blue) do not produce notably different best-fit parameters than other Mach numbers. The conduction runs that produce the highest N_0 and lowest q have moderate Mach numbers, between 3 and 4 (shown in green). This degeneracy is likely due to the fact that the compression for the conduction runs is less significant at higher Mach numbers, allowing for clouds to develop a dense outer layer but an interior with a lower density, ultimately reducing the overall column densities.

The dependence of parameters on velocity is shown in Figure 5. Here there is a similar trend to the low Mach numbers, where low velocities (those below 1000 km s^{-1}) produce the lowest of the fits for N_0 and q . The highest velocities result in the maximum N_0 for both cooling and conduction and the trend arrows for both efficient and inefficient conduction appear to follow the general shape of the data. High velocities also correspond to high q values, reflecting the effects of shocks on both the cloudlets within a cooling run and the filaments in the conduction runs to compress the gas.

5. Application: Down-the-barrel Outflow Observations

As an illustration of the types of studies enabled by our results, we consider an application of our tabulated fits. We consider the observations in Chisholm et al. (2018) in particular as many of our assumptions, including radiation background and ionization parameter, are derived from these observations. Chisholm et al. (2018) report absorption profiles from down-the-barrel observations, of a lensed galaxy with $z \approx 2.9$. Observations are made of both low and high ionization profiles

that indicate that the two phases are cospatial, much like the wind-cloud interaction considered here. We aim to determine an appropriate scaling of our column density profiles by accounting for two factors that can influence the optical depth of the absorbing clouds.

To approximate an absorption profile for these ions, we estimate the observed optical depth for a particular ion as

$$\tau(v) = \frac{c\sigma}{\sqrt{\pi}b} \exp\left[-\frac{(v-v_0)^2}{b^2}\right] \bar{N}, \quad (16)$$

where $\bar{N} \equiv \frac{\sum_i N_i}{x}$, is the average number density of the ion, where x is the number of points within the column density profile and N_i is the column density for the i th point. Here τ is approximated with the center of the absorption profile at the average velocity of the cloud, v_0 , with a velocity dispersion determined by the b parameter estimated for each ion, and v is the velocity bin within the absorption profile. We consider velocities between -600 and 200 km s^{-1} offset from line center. This average optical depth approximates a single cloud.

There are then two ways to parameterize the absorption profile, we consider the two parameters independently. The first method is altering covering fraction, which describes the fraction of the area within the sightline that is obscured by the cloud. With this covering fraction parameter, the observed flux from the derived column density profiles can be expressed as

$$F(v) = (1 - f) + fe^{-\tau(v)}, \quad (17)$$

where $\tau(v)$ is the average optical depth above and f is the free parameter describing the covering fraction.

The second way to parameterize the absorption profile considers scaling the optical depth either to represent multiple clouds along the sightline or one cloud with scaled density. For this, we assume that the intervening cloud has the average optical depth of a single cloud from Equation (16), which is then scaled by the parameter α , which describes the number of clouds within the sightline or the scaling factor of the density for a single cloud. In this case, the observed flux can be described as

$$F(v) = e^{-\alpha\tau(v)}, \quad (18)$$

where $\tau(v)$ is again the average optical depth above and α is the second free parameter we consider, describing the number of clouds.

Best-fit covering fraction and α are found by performing χ^2 minimizations for each of the parameters independently over the five ions shared between our analysis and the Chisholm et al. (2018) observations, C II, C IV, Si IV, O VI, and N V. We determine this χ^2 for each of the four evolutionary stages, which here correspond to a central velocity, for all of the 22 runs.

The best fit for both approaches, each with their own free parameter, is shown in Figure 6, with the covering fraction fits in red and the multcloud fits in blue. Also shown with dashed lines are the $\alpha = 1$ and $f = 1$ cases, highlighting the profiles produced with the base case of one cloud with full coverage over the sightline. The run with the best fit for the covering fraction case is M3.5-v1700-T1-c with a covering fraction of 0.621. The covering fraction approach is able to generate profiles that approximate the nearly saturated lines Si IV and C IV, and maintain the low levels of N V to match observations in Chisholm et al. (2018). However, there is not enough C II or

O VI in our simulations to reproduce the observed profiles with a single cloud.

In the case in which the optical depth is increased uniformly and parameterized by the number of clouds, we find a best-fit α of 488 for the best-fit run M3.6-v3000-T3-hc. It is important to acknowledge that it is highly unlikely that 488 clouds would be lined up to each fully cover a particular sightline, though scaling the density of one cloud by this factor is feasible. However, this number, paired with the fact that this best-fit run is one of the high column density runs, demonstrates that there is a significant discrepancy between these simulations and the observations. In particular, our simulations do not produce enough C II. While Si IV and C IV are saturated in the base case and more clouds only widen the profile, the low levels of C II drive up the number of clouds necessary in order to approach the nearly saturated C II observations.

For the intermediate ions, Si IV, C IV, and C II, it is also clear that the derived line widths are much narrower than those observed in Chisholm et al. (2018). This limits the simulations' potential to produce these wide profiles by simply altering the optical depth. However, for O VI, there is an opposite effect. While most of the high column density O VI is found on the interface of the cloud, there is a portion of O VI that can be found in the hot wind (see Figures 1 and 2). This gives O VI velocity dispersions on the order of the wind velocity, 10^3 km s^{-1} . This can account for the nearly flat appearance of the best-fit for the multiple cloud approach in O VI. The shallow and wide profile appears flat over the range of velocities relevant for the other ions. Even so, there is not enough O VI within or on the interfaces of the slower moving cloud to reproduce the deep profiles observed. It is possible that this discrepancy could be explained by the effects of low resolution. However, Table 4 shows the best-fit parameters for O VI, within a higher resolution cooling run. O VI would be most affected by resolution effects due to the fact it is produced within mixing layers. The higher resolution run produces comparable maximum column densities and similar coverage parameters, q , to the run with the resolution used throughout the rest of the simulations.

Ultimately, a more realistic view would treat both of these factors together, introducing the influence of a density scaling or multiple clouds each with their own covering fraction. However, these simplistic views can support the need for further investigation. While comparable amounts of Si IV and C IV absorption can be recreated, the lack of C II indicates that there is a significant factor not accounted for that enables more cold cloud material to remain within the sightline throughout the interaction with the wind. The wide velocity dispersions of O VI also indicate a need to determine a source of O VI ionization that can introduce noticeable absorption over a smaller velocity range.

6. Discussion and Summary

Starburst-driven galactic outflows are a complex, multiphase phenomenon, and understanding their evolution requires close comparisons between observations and numerical studies. While numerical simulations can reproduce the full evolution of cold clouds interacting with hot wind material given a set of assumptions about the underlying physical processes, observations are often limited to absorption line profiles of species with low and intermediate ionization states.

To help in interpreting such observations, we have derived equilibrium column density profiles, average velocities, and b parameters for 22 hydrodynamical simulations of cold, atomic clouds in supersonic winds, including both radiative cooling and thermal conduction. These capture the equilibrium distributions of 10 widely observed ions: H I, Mg II, C II, C III, C IV, Si III, Si IV, N V, O VI, and Ne VIII. With the possible exception of H I, the column density profiles are all well fit by the functional form $N(x) = N_0 \frac{0.01}{1.01 - x^q}$, where x is the fractional rank of each cell expressed as a fraction of the total, N_0 places an upper limit on column density and q expresses the degree to which the cloud has been compacted. For all ions, we provide tabulated fits of N_0 and q for each simulation case, at four characteristic times.

As a general trend, the runs including conduction produce much higher column densities and much narrower amounts of coverage, coinciding with the more compact, dense filaments produced in late stages of the cloud–wind interaction. The runs with inefficient conduction are restricted to lower column densities for most ions except N V and O VI, which are primarily produced at the cloud–wind boundary. These runs also follow more predictable trends with functions of wind velocity and Mach number as higher velocities compact the cloud and result in higher column densities.

Our study is limited by the need to reduce the parameter space with the assumption that the metallicity is solar. While this is an estimate of the maximum metallicity within the CGM, the absorption observed near starbursts is more likely due to high amounts ion ionization rather than high metal content. We also assume a radiation model representative of a young starburst galaxy at a high ionization parameter ($\log U = -2$), which can greatly vary between CGM observations and is a necessary component to making connections to CGM observations such as COS-Burst.

However, even in comparison to observations that best match our assumed parameters, we find that we cannot reproduce observed absorption line column density ratios with our equilibrium model. Our results overestimate the amounts of intermediate ions such as Si IV and C IV, as they produce saturated profiles. Due to this, the best-fit parameters that produce fits that closely match the profiles for Si IV and C IV also significantly underestimate the absorption from O VI, N V, and C II. The discrepancy between O VI and N V absorption is

also not explained by the inclusion of thermal conduction. In both cases, inefficient and efficient conduction, the column densities of both ions are comparable and not impacted by resolution effects. Thus it is possible that the lack of N V observed is linked to nonequilibrium processes (e.g., Grassi et al. 2014; Gray et al. 2015; Gray & Scannapieco 2016, 2017; Pallottini et al. 2017), which must be accounted for through the use of a full chemical network.

Addressing this issue will require performing a similar analysis on outflow simulations including nonequilibrium chemistry. These can then be compared with the present fits to demonstrate the drawbacks of the equilibrium assumption, and they will yield better estimates of the abundances of each ion. Other consideration should be given to the effects of different ionization parameters and metallicities that are more descriptive of the CGM, as well as the balance between cooling and potential photo-heating. These parameters are likely to have a significant effect on the production of low ions in particular. Similarly, simulations including other effects such as the impact of magnetic fields and cosmic rays (e.g., Simpson et al. 2016; Ruszkowski et al. 2017; Fujita & Mac Low 2018; Samui et al. 2018), as well as addressing the contribution of cold gas created in the expanding wind (e.g., Thompson et al. 2016; Scannapieco 2017; Schneider et al. 2018) will likely be needed to fully address the parameter space of the physical process impacting galactic outflows, their interaction with the CGM, and their influence on galaxy evolution.

This work was supported by the National Science Foundation under grant AST14-07835 and NASA theory grant NNX15AK82G. We would like to thank John Chisholm, Sanchayeeta Borthakur, and Neal Katz for informative and helpful discussions as well as Cameron Hummels and Britton Smith for advice regarding the use of TRIDENT. E.S. gratefully acknowledges the Simons Foundation for funding the workshop Galactic Winds: Beyond Phenomenology, which helped to inspire this work. We would also like to thank the Texas Advanced Computing Center (TACC) at The University of Texas at Austin, and the Extreme Science and Engineering Discovery Environment (XSEDE) for providing HPC resources via grant TGAST130021 that have contributed to the results reported within this paper. M.B. is supported by a grant by the Deutsche Forschungsgemeinschaft under BR2026125.

Appendix

Table 4

Best-fit N_0 and q for the High-resolution Run at Each Stage

	M3.5-v1700-T1	M3.5-v1700-T1-highres
q_1	-1.756	-1.804
q_2	-1.820	-2.097
q_3	-1.583	-1.848
q_4	-1.272	...
$\log(N_{0,1})$	14.208	14.040
$\log(N_{0,2})$	14.328	14.165
$\log(N_{0,3})$	14.588	14.275
$\log(N_{0,4})$	14.490	...

ORCID iDs

Evan Scannapieco  <https://orcid.org/0000-0002-3193-1196>

References

- Agertz, O., & Kravtsov, A. V. 2015, *ApJ*, **804**, 18
- Arav, N., Borguet, B., Chamberlain, C., Edmonds, D., & Danforth, C. 2013, *MNRAS*, **436**, 3286
- Arribas, S., Colina, L., Bellocchi, E., Maiolino, R., & Villar-Martín, M. 2014, *A&A*, **568**, A14
- Bolatto, A. D., Warren, S. R., Leroy, A. K., et al. 2013, *Natur*, **499**, 450
- Borthakur, S., Heckman, T., Strickland, D., Wild, V., & Schiminovich, D. 2013, *ApJ*, **768**, 18
- Brüggen, M., & Scannapieco, E. 2016, *ApJ*, **822**, 31
- Calzetti, D., Armus, L., Bohlin, R. C., et al. 2000, *ApJ*, **533**, 682
- Chevalier, R. A., & Clegg, A. W. 1985, *Natur*, **317**, 44
- Chisholm, J., Bordoloi, R., Rigby, J. R., & Bayliss, M. 2018, *MNRAS*, **474**, 1688
- Colella, P., & Woodward, P. R. 1984, *JCoPh*, **54**, 174
- Cowie, L. L., & McKee, C. F. 1977, *ApJ*, **211**, 135
- Creasey, P., Theuns, T., & Bower, R. G. 2013, *MNRAS*, **429**, 1922
- Dalla Vecchia, C., & Schaye, J. 2008, *MNRAS*, **387**, 1431
- Davé, R., Finlator, K., & Oppenheimer, B. D. 2011, *MNRAS*, **416**, 1354
- Dekel, A., & Silk, J. 1986, *ApJ*, **303**, 39
- Ferland, G. J., Porter, R. L., van Hoof, P. A. M., et al. 2013, *RMxAA*, **49**, 137
- Ford, A. B., Oppenheimer, B. D., Davé, R., et al. 2013, *MNRAS*, **432**, 89
- Foreman-Mackey, D., Hogg, D. W., Lang, D., & Goodman, J. 2013, *PASP*, **125**, 306
- Fragile, P. C., Anninos, P., Gustafson, K., & Murray, S. D. 2005, *ApJ*, **619**, 327
- Fryxell, B., Olson, K., Ricker, P., et al. 2000, *ApJS*, **131**, 273
- Fujita, A., & Mac Low, M.-M. 2018, *MNRAS*, **447**, 531
- Grassi, T., Bovino, S., Schleicher, D. R. G., et al. 2014, *MNRAS*, **439**, 2386
- Gray, W. J., & Scannapieco, E. 2010, *ApJ*, **718**, 417
- Gray, W. J., & Scannapieco, E. 2016, *ApJ*, **818**, 198
- Gray, W. J., & Scannapieco, E. 2017, *ApJ*, **849**, 132
- Gray, W. J., Scannapieco, E., & Kasen, D. 2015, *ApJ*, **801**, 107
- Gronke, M., & Oh, S. P. 2018, *MNRAS*, **480**, 111
- Haart, T., & Madau, P. 2012, *ApJ*, **746**, 125
- Heckman, T., Borthakur, S., Wild, V., Schiminovich, D., & Bordoloi, R. 2017, *ApJ*, **846**, 151
- Heckman, T. M., Armus, L., & Miley, G. K. 1990, *ApJS*, **74**, 833
- Hopkins, P. F., Quataert, E., & Murray, N. 2012, *MNRAS*, **421**, 3522
- Hummels, C. B., Smith, B. D., & Silvia, D. W. 2017, *ApJ*, **847**, 59
- Kacprzak, G. G., Martin, C. L., Bouché, N., et al. 2014, *ApJL*, **792**, L12
- Kaviraj, S., Laigle, C., Kimm, T., et al. 2017, *MNRAS*, **467**, 4739
- Keeney, B. A., Stocke, J. T., Rosenberg, J. L., et al. 2013, *ApJ*, **765**, 27
- Klein, R. I., McKee, C. F., & Colella, P. 1994, *ApJ*, **420**, 213
- Kwak, K., Henley, D. B., & Shelton, R. L. 2011, *ApJ*, **739**, 30
- Leitherer, C., Schaerer, D., Goldader, J. D., et al. 1999, *ApJS*, **123**, 3
- Lu, Y., Blanc, G. A., & Benson, A. 2015, *ApJ*, **808**, 129
- Mac Low, M.-M., & Ferrara, A. 1999, *ApJ*, **513**, 142
- Mac Low, M.-M., McKee, C. F., Klein, R. I., Stone, J. M., & Norman, M. L. 1994, *ApJ*, **433**, 757
- Martin, C. L. 1999, *ApJ*, **513**, 156
- Martin, C. L. 2005, *ApJ*, **621**, 227
- McCarthy, P. J., van Breugel, W., & Heckman, T. 1987, *AJ*, **93**, 264
- McCourt, M., O'Leary, R. M., Madigan, A.-M., & Quataert, E. 2015, *MNRAS*, **449**, 2
- McKeith, C. D., Greve, A., Downes, D., & Prada, F. 1995, *A&A*, **293**, 703
- Meiring, J. D., Tripp, T. M., Werk, J. K., et al. 2013, *ApJ*, **767**, 49
- Morel, J. E. 2000, *JQST*, **65**, 769
- Mori, M., Ferrara, A., & Madau, P. 2002, *ApJ*, **571**, 40
- Muratov, A. L., Kereš, D., Faucher-Giguère, C.-A., et al. 2015, *MNRAS*, **454**, 2691
- Murray, N., Ménard, B., & Thompson, T. A. 2011, *ApJ*, **735**, 66
- Oppenheimer, B. D., & Davé, R. 2006, *MNRAS*, **373**, 1265
- Oppenheimer, B. D., Davé, R., & Finlator, K. 2009, *MNRAS*, **396**, 729
- Oppenheimer, B. D., Davé, R., Kereš, D., et al. 2010, *MNRAS*, **406**, 2325
- Orlando, S., Peres, G., Reale, F., et al. 2005, *A&A*, **444**, 505
- Pallottini, A., Ferrara, A., Bovino, S., et al. 2017, *MNRAS*, **471**, 4128
- Rubin, K. H. R., Prochaska, J. X., Koo, D. C., et al. 2014, *ApJ*, **794**, 156
- Ruszkowski, M., Yang, H.-Y. K., & Zweibel, E. 2017, *ApJ*, **834**, 208
- Samui, S., Subramanian, K., & Srianand, R. 2018, *MNRAS*, **476**, 1680
- Scannapieco, E. 2017, *ApJ*, **837**, 28
- Scannapieco, E., & Broadhurst, T. 2001, *ApJ*, **549**, 28
- Scannapieco, E., & Brüggén, M. 2015, *ApJ*, **805**, 158
- Scannapieco, E., Ferrara, A., & Madau, P. 2002, *ApJ*, **574**, 590
- Scannapieco, E., & Oh, S. P. 2004, *ApJ*, **608**, 62
- Scannapieco, E., Thacker, R. J., & Davis, M. 2001, *ApJ*, **557**, 605
- Schaye, J., Crain, R. A., Bower, R. G., et al. 2015, *MNRAS*, **446**, 521
- Schneider, E. E., & Robertson, B. E. 2017, *ApJ*, **834**, 144
- Schneider, E. E., Robertson, B. E., & Thompson, T. A. 2018, *ApJ*, **862**, 56
- Shapley, A. E., Steidel, C. C., Pettini, M., & Adelberger, K. L. 2003, *ApJ*, **588**, 65
- Sijacki, D., Springel, V., Di Matteo, T., & Hernquist, L. 2007, *MNRAS*, **380**, 877
- Simpson, C. M., Pakmor, R., Marinacci, F., et al. 2016, *ApJL*, **827**, L29
- Smith, B., Sigurdsson, S., & Abel, T. 2008, *MNRAS*, **385**, 1443
- Smith, B. D., Bryan, G. L., Glover, S. C. O., et al. 2017, *MNRAS*, **466**, 2217
- Springel, V., & Hernquist, L. 2003, *MNRAS*, **339**, 289
- Sturm, E., González-Alfonso, E., Velleux, S., et al. 2011, *ApJL*, **733**, L16
- Thompson, T. A., Quataert, E., Zhang, D., & Weinberg, D. H. 2016, *MNRAS*, **455**, 1830
- Tremonti, C. A., Heckman, T. M., Kauffmann, G., et al. 2004, *ApJ*, **613**, 898
- Turk, M. J., Smith, B. D., Oishi, J. S., et al. 2011, *ApJS*, **192**, 9
- Turner, M. L., Schaye, J., Crain, R. A., Theuns, T., & Wendt, M. 2016, *MNRAS*, **462**, 2440
- Vielleux, S., Cecil, G., & Bland-Hawthorn, J. 2005, *ARA&A*, **43**, 769
- Werk, J. K., Prochaska, J. X., Cantalupo, S., et al. 2016, *ApJ*, **833**, 54
- Werk, J. K., Prochaska, J. X., Tumlinson, J., et al. 2014, *ApJ*, **792**, 8
- Wiersma, R. P. C., Schaye, J., & Smith, B. D. 2009, *MNRAS*, **393**, 99
- Wiseman, P., Perley, D. A., Schady, P., et al. 2017, *A&A*, **607**, A107